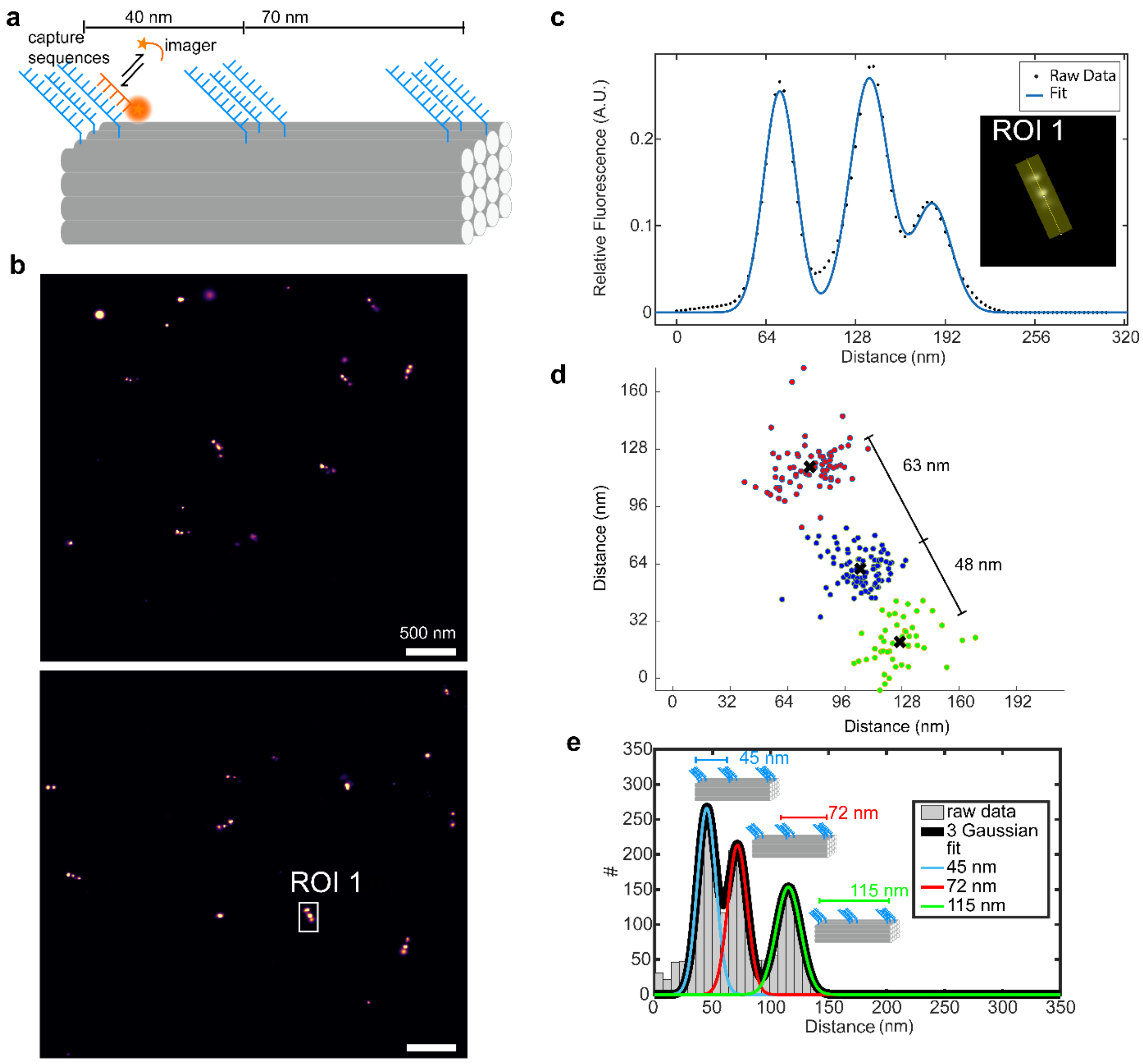

Supplementary Figure 1: Imaging DNA origami via DNA-PAINT. (**a**) Schematic of 16-helix bundle DNA origami standard with nine docking sites clustered in groups of three. Sites were spaced 40 and 70 nm apart. (**b**) Origami were attached to the surface by biotin-streptavidin. Upon the addition of 2.5 nM Cy3B imager, single molecule fluorescence localizations were observed. Integrating 3000-5000 frames revealed origamis adhered to the surface with the characteristic 3 linearly spaced docking sequences. Note that not all origamis were completely assembled. These images are representative of *n* = 3 experiments. (**c**) Linescan analysis of a grayscale rendering of the indicated origami (white box b-i) revealed 3 spots. (**d**) The individual single-molecule localizations of one origami indicated in the white box were subjected to k-means analysis to cluster the localizations into 3 clusters. The centroids of these clusters were separated by 63 and 48 nm. This analysis was duplicated to ~550 origami from *n* = 3 surfaces. (**e**) This k-means analysis was applied to ~550 origami from *n* = 3 surfaces. The histogram shows the distribution of differences between the 3 clusters identified by the k-means analysis on those 550 origami from n = 3 surfaces. The fit curve depicts the sum of 3 gaussians with centroids separated by 46, 73, and 115 nm. The individual gaussians are also rendered (colored lines in **e**). The distances between these centroids fit well to the expected values.

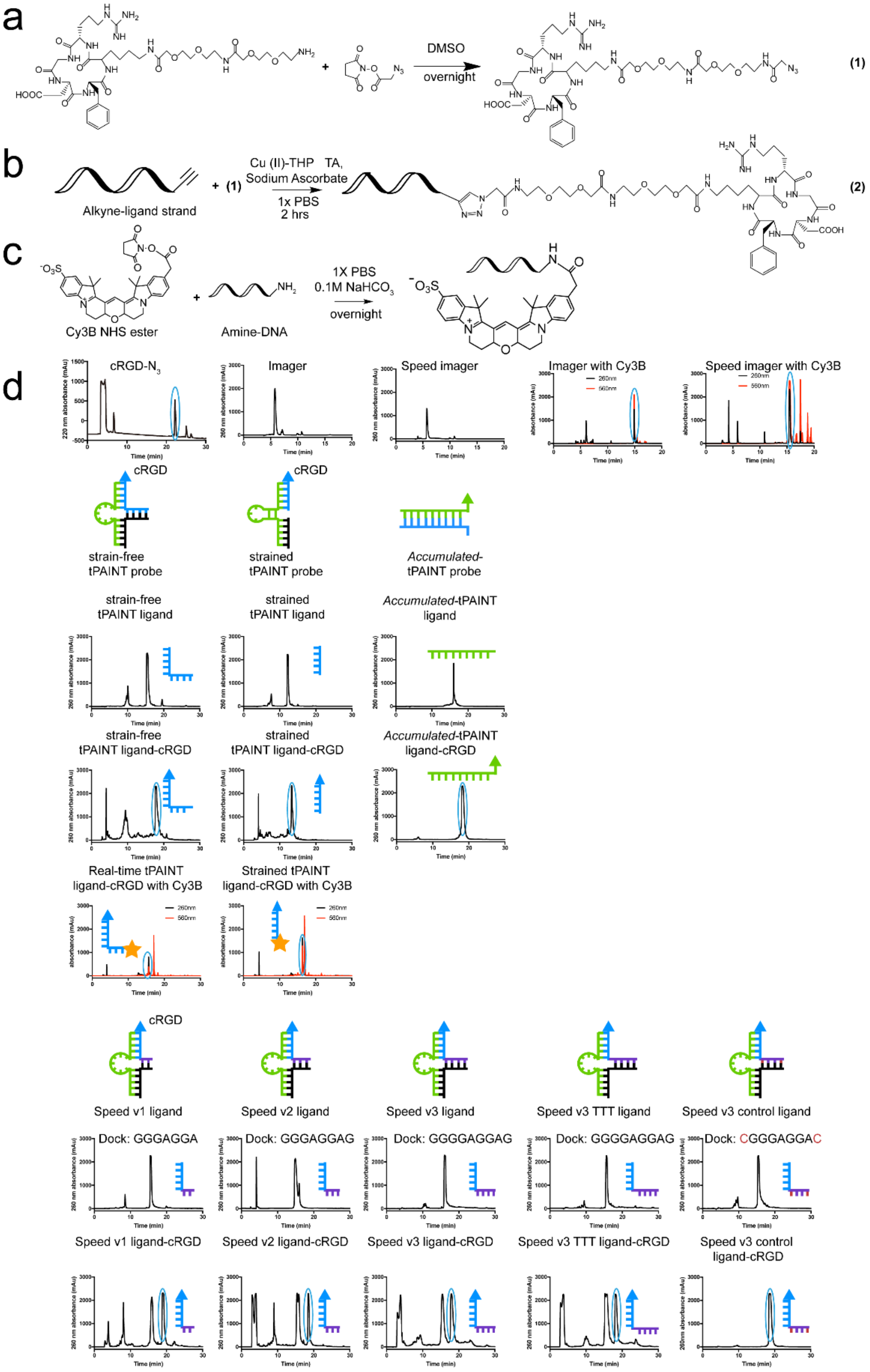

Supplementary Figure 2: HPLC Characterization of tPAINT Probes. (caption continues on next page)

Supplementary Figure 2, continued (**a**) Schematic showing the coupling between NHS-N_3 and cRGDfK-PEG-PEG-NH_2 to form cRGD-PEG-PEG -N_3. (**b**) Alkyne-azide cycloaddition reaction to conjugate cRGD peptide to the DNA. (**c**) Schematic of showing coupling of Cy3B-NHS to DNA. (**d**) HPLC spectra of the all the starting material (cRGD and oligonucleotides) as well as the products generated in this work. Chromatograms of the starting materials were used to confirm the purity of the oligonucleotides custom synthesized by IDT. The products of the cRGD and dye coupling reactions were purified using HPLC and the peaks identified with the blue circles indicate the materials that was used for subsequent steps. Solvent program for peptides: 1mL/min flow rate: Solvent A: nanopure water + 0.05% TFA, Solvent B: acetonitrile + 0.05% TFA; starting condition: 90% A + 10 % B, 1%/min gradient B. Solvent program for DNA: 0.5 mL/min flow rate; Solvent A: 0.1M TEAA, Solvent B: acetonitrile; starting condition: 90% A + 10 % B, 0.5%/min gradient B. The retention times of all starting reagents and products are given in **Supplementary Table 2.**

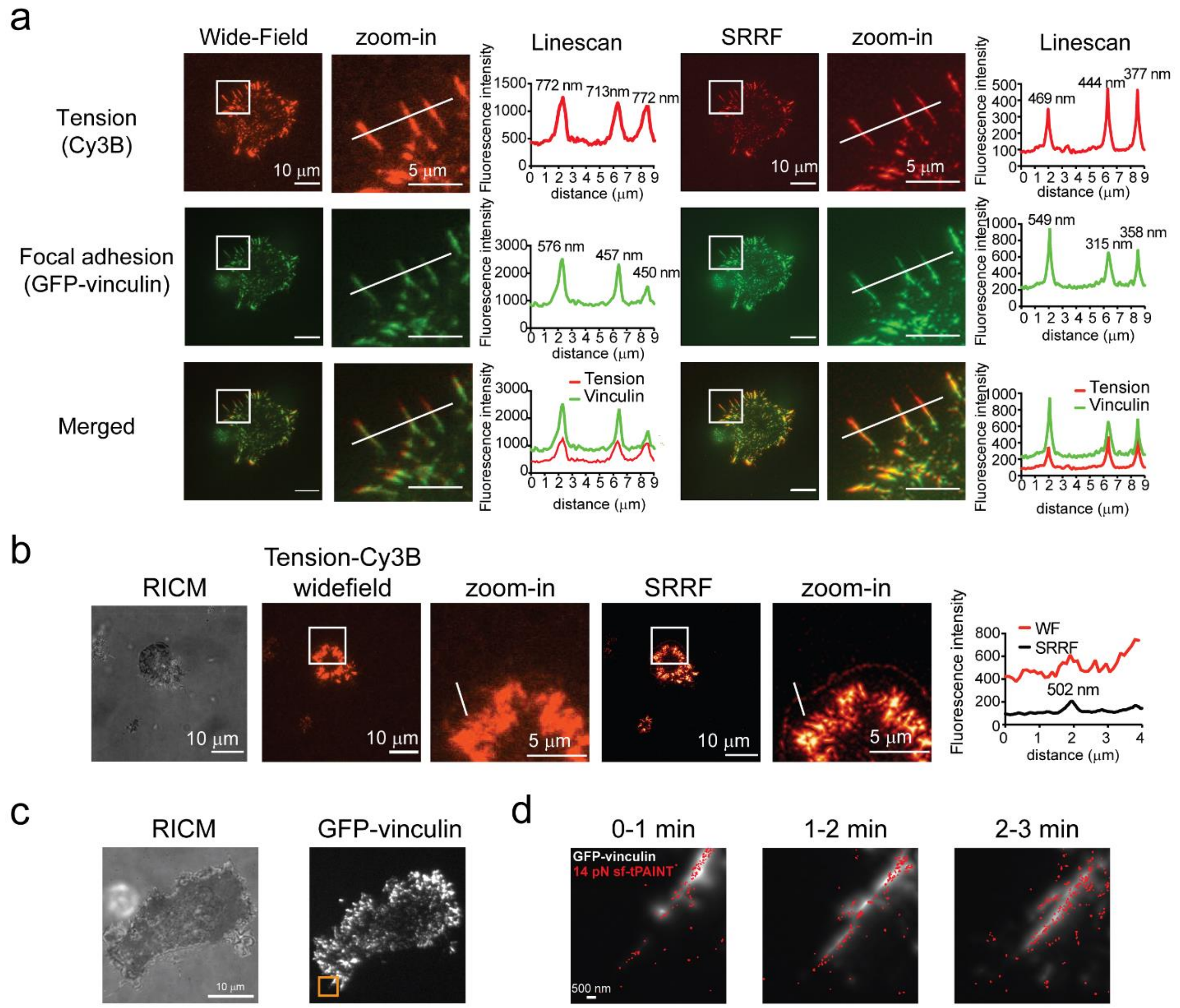

Supplementary Figure 3: Turn-on fluorescence signal and super-resolved radial fluctuations (SRRF) of sf-tPAINT tension probes. (**a**) tPAINT tension probes (**Fig. 1a**) modified with a Cy3B-BHQ2 fluorophore-quencher produce a turn-on fluorescence signal using MEF GFP-vinculin cells and (**b**) human platelets. Super-resolved imaging via super resolution radial fluctuations (SRRF)[1] was also performed on this data and representative line scans are shown to the right of each set of images. The value above each peak in the line scan shows the FWHM of the tension generating structures. Note that vinculin colocalizes with the tension signal **(a)** as previously reported[2, 3]. The results shown are representative of *n* = 2 fibroblasts experiments and *n* = 1 human platelet experiment. **(c)** RICM and TIRF images of mouse embryonic fibroblast cell expressing GFP-vinculin. **(d)** Zoom in showing an overlay of 14 pN sf-tPAINT (shown in red) and SRRF of GFP-vinculin (gray). The three frames show the dynamic nature of the projection and how the 14 pN traction forces change during the 3 min interval. SRRF-tPAINT images are representative of 2 independent experiments.

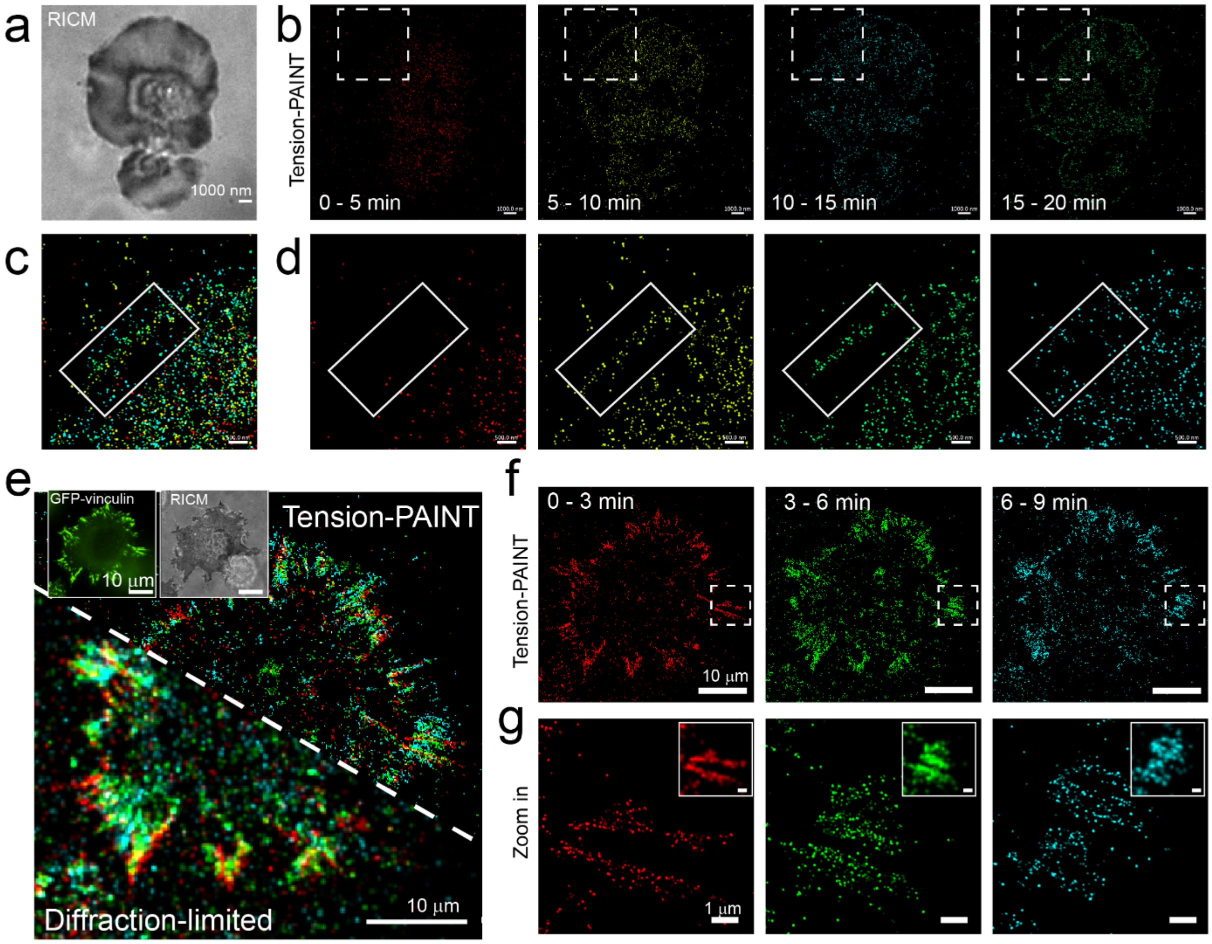

Supplementary Figure 4: Time-resolved tPAINT for MEFs and platelets in cell culture media. (**a**) RICM and (**b**) time resolved 7.3pN sf-tPAINT of human platelets performed in Tyrode's buffer using the strain-free tPAINT probe and 10nM Cy3B imager. (**c-d**) Zoom-in of dotted box in (**b**) focusing on platelet lamellipodial edge tension. The white box in (d) provides a frame of reference showing the movement of the edge tension. Note that significantly fewer single molecule localizations are observed in Tyrode's media compared to Tyrode's media supplemented with 37.5mM Mg^{2+} (**Fig. 1** and **Extended Data Fig. 2, 3**). (**e**) RICM, GFP-vinculin, and 8pN sf-tPAINT of MEF cell spreading in cell culture media (fluorobrite-DMEM, supplemented with 0.5-1% heat-inactivated fetal bovine serum). (**f**) Focal adhesion dynamics are visible in time-resolved sf-tPAINT. (**g**) Magnified view of the dotted box region in f. Insets depict the diffraction limited reconstruction of the super-resolved single molecule localizations in **g**. Data shown is representative of *n* = 4 platelet experiments and *n* = 3 fibroblast experiments. Additional example images are provided in **Extended Data Fig. 2**.

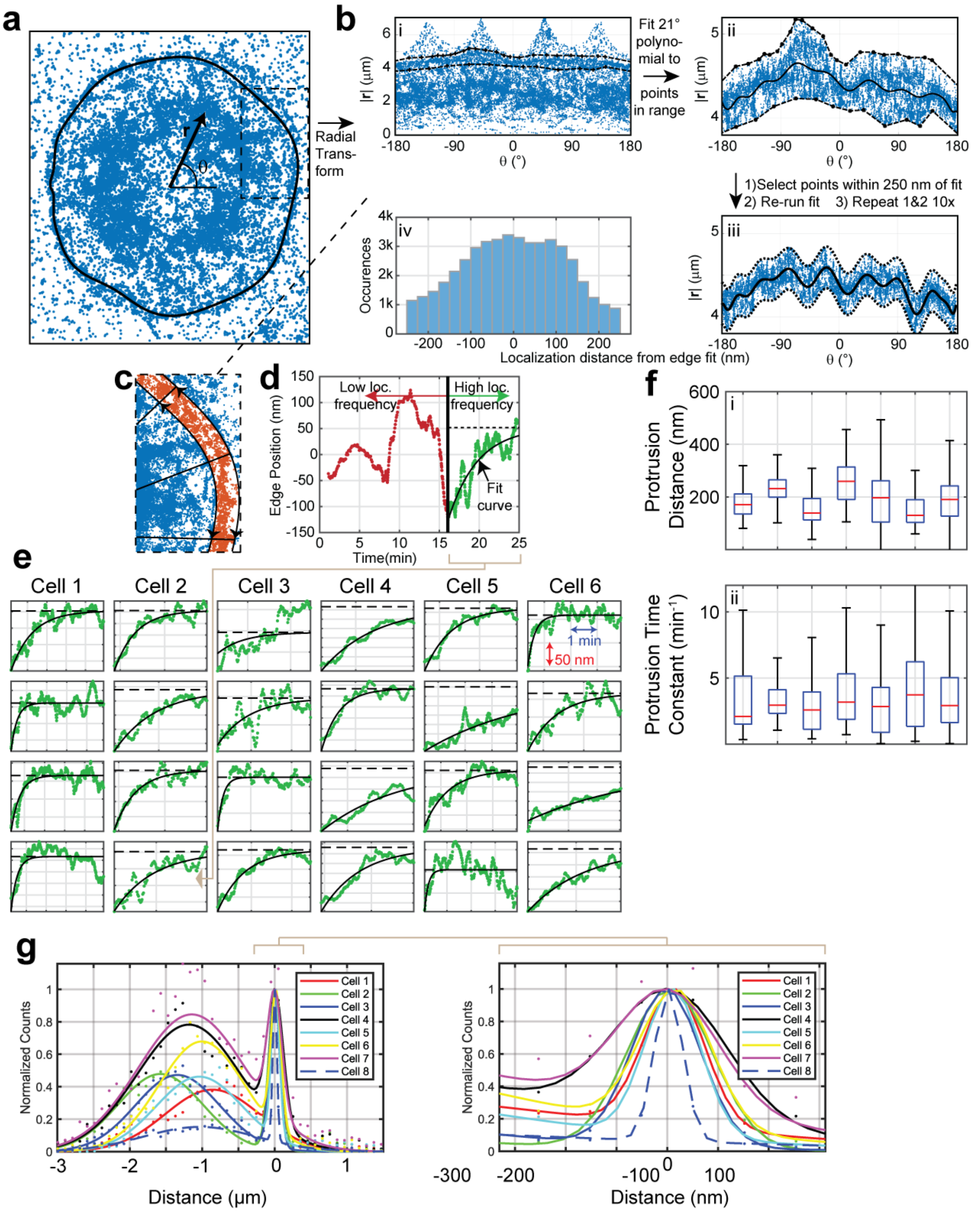

Supplementary Figure 5: Analysis of platelet lamellipodial tension dynamics. The analysis presented in this figure is based on the 8.5pN sf-tPAINT probe in 37.5 mM $MgCl_2$, where the tension signal of six platelets (from *n* = 3 independent biological replicates) that exhibited clear spreading behavior was analyzed. (caption continues on next page)

Supplementary Figure 5, continued (**a**) Scatter plot of 10% of the 8.5pN sf-tPAINT localizations (to enable facile visualization) showing the tension footprint of a human platelet 20-30 min after seeding the cells. A radial coordinate system was established from the cell centroid (vector **r** and angle θ). The black contour denotes the approximate lamellipodial edge position. (**b**) The lamellipodial edge contour was calculated using a semi-interactive algorithm: i) First, the localization data shown in (**a**) was transformed to a radial coordinate system, and the interactive MATLAB function "getpts()" was used to obtain a user-drawn polygon (denoted with black dashed lines with + symbols on vertices) around the high localization-density region corresponding to the edge of the cell. ii) A 21st-order polynomial was then fit to the localizations within this polygon (shown as solid black line). iii) To reduce user-bias, the polygon was then discarded and all localization (including some that were not in the original polygon) within a 250 nm cutoff of the fit-polynomial were selected and a new 21st-order polynomial was fit to the localizations. This process was repeated ten times to ensure convergence to an optimal polynomial. This polynomial function was taken as the cell boundary as shown in (**a**). iv) The distances of all localizations within 250 nm of the final contour was constructed. (**c**) With this radial coordinate system, a series of wedge-shaped regions of interest with 45°-wide slices were created and rotated around the origin in 1° increments. Localizations within 250 nm of the boundary in that slice are isolated for analysis. (**d**) The edge position of the lamellipodium in that slice is then quantified as a function of time by sorting localizations by the time they occurred and their radial position relative to the cell edge (black line) as shown in figure **b**-iv. To measure dynamics, a temporal sliding window of 250 localizations per wedge was employed. The data shown corresponds to the 45° slice centered on θ=21° for cell 2 shown in (**c**). We found that the localization frequency (inset) was generally very low at early time points (red), but then sharply increased following the rapid formation of a well-defined lamellipodial edge (green). For the cell shown, localization frequency was ~2 s^{-1}, but increased to a sustained rate of ~8 s^{-1} within the platelet footprint at ~15 min (indicated by the black arrow in the inset), which was taken as the onset of lamellipodial edge tension and spreading. Prior to edge-formation, the measured edge position was random (likely the result of random noise and uncoordinated activity by the cell), but following edge-formation the edge position typically spiked sharply (due to the rapid increase in localization frequency at the inner-edge of the ROI) and moved outwards in an asymptotic manner. To quantify the dynamics of lamellipodial outward edge migration, we fit the edge position (R) vs. time (t) data to a decaying exponential function: position = $c-a*\exp[(t-t_0)/\tau]$), where τ, a, and c (which correspond to the protrusion time constant, the protrusion distance, and the final edge position, respectively) are all free fit parameters and t_0 (the time of edge formation) is obtained by finding the time point at which edge position is minimized. In (**d**), t_0 is denoted using a thick black line, and the fit curve is shown with a black curve. The best-fit c value is denoted using a dashed line. (**e**) For each of the six cells, calculated edge position data and fit curves are shown for $t > t_0$ for four non-overlapping 45° slices. For all but a few of the fits shown, the exponential decay fit accurately describes the observed data. (**f**) Compilation of all best-fit parameters – except when an error occurring during the fitting algorithm due to poor fit-quality – enables population-level quantification of the dynamic and structural properties of the platelets studied. For cells 1-6, 343, 270, 213, 302, 318, and 308 slices, respectively, were analyzed using the fully-automated process described in **d** & **e**. Boxplots showing the populations of best-fit i) a values and ii) τ values are shown for each of the six cells. For these box and whisker plots the red bar is the median, the bounds of the box mark the 25th and 75th percentile (interquartile range), and the maxima/minima of the whiskers extend 1.5 interquartile ranges away from the boundaries of the box. Outliers, which are defined as points that lie more than 1.5 interquartile ranges outside the 25th/75th percentiles, are not shown. Boxplots reflecting a merged dataset with all six cells are also shown. Median protrusion values (red horizontal line) ranged from 130 nm to 260 nm, with the compiled dataset having a median of 190 nm. Median τ values ranged from 2.1 min to 3.7 min, with the compiled dataset having a median of 2.9 min. (**g**) To calculate the width of the platelet lamellipodial edge, the localizations of a set of spread, static platelets corresponding to the single-molecule sf-tPAINT data from 1000 frames (collected at 5Hz) were fit to a 21st order polynomial as in (**a**). The distance of all localizations from this 21st order polynomial was calculated and plotted in a histogram (**g**). Zero in (**g**) represents the location of the 21st order polynomial, negative distances are towards the center of the platelet, while positive distances are towards the edge of the platelet. This analysis reveals a bimodal distribution of single-molecule localizations, a peak near the center of the platelet and a peak at the cell edge. The full width half maximum (FWHM) of 8 platelets (*n* = 3 independent experiments) was calculated in this way. The average FWHM is 150 +/- 80 nm (mean +/- standard deviation).

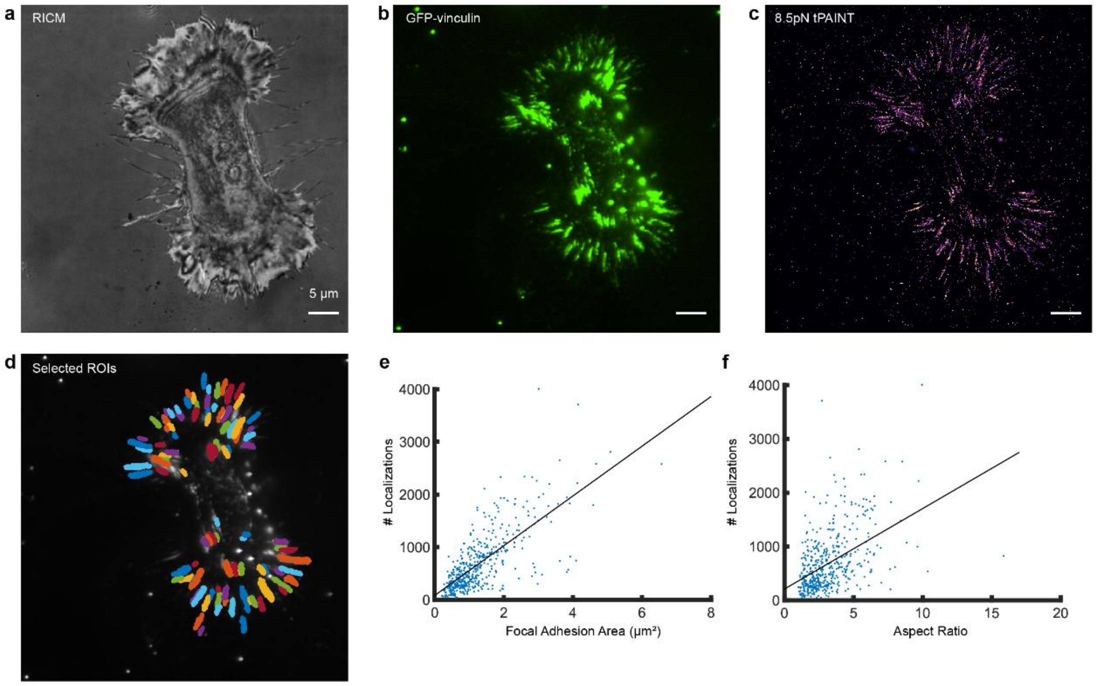

Supplementary Figure 6: The number of 8.5pN tPAINT localizations per adhesion is positively correlated with focal adhesion area and aspect ratio. (**a**) RICM, (**b**) GFP-vinculin, and (**c**) 8.5 pN sf-tPAINT image for a MEF-GFP-vinculin cell. (**d**) Regions of interest corresponding to focal adhesions were manually identified from tPAINT localizations and GFP-vinculin fluorescence. The ROIs identified for this cell are plotted in different colors in (**d**). (**e**) Scatterplot of focal adhesion area versus the number of localizations within that area. Localization number is positively correlated with focal adhesion area, R = 0.72. (**f**) Focal adhesion aspect ratio versus localization number. The aspect ratio was denoted by fitting an ellipse to the region of interest and taking the ratio of the major to minor axes. Aspect ratio is weakly correlated to localization number, R = 0.46. In total, 483 focal adhesions from 5 cells (*n* = 3 independent experiments) were analyzed.

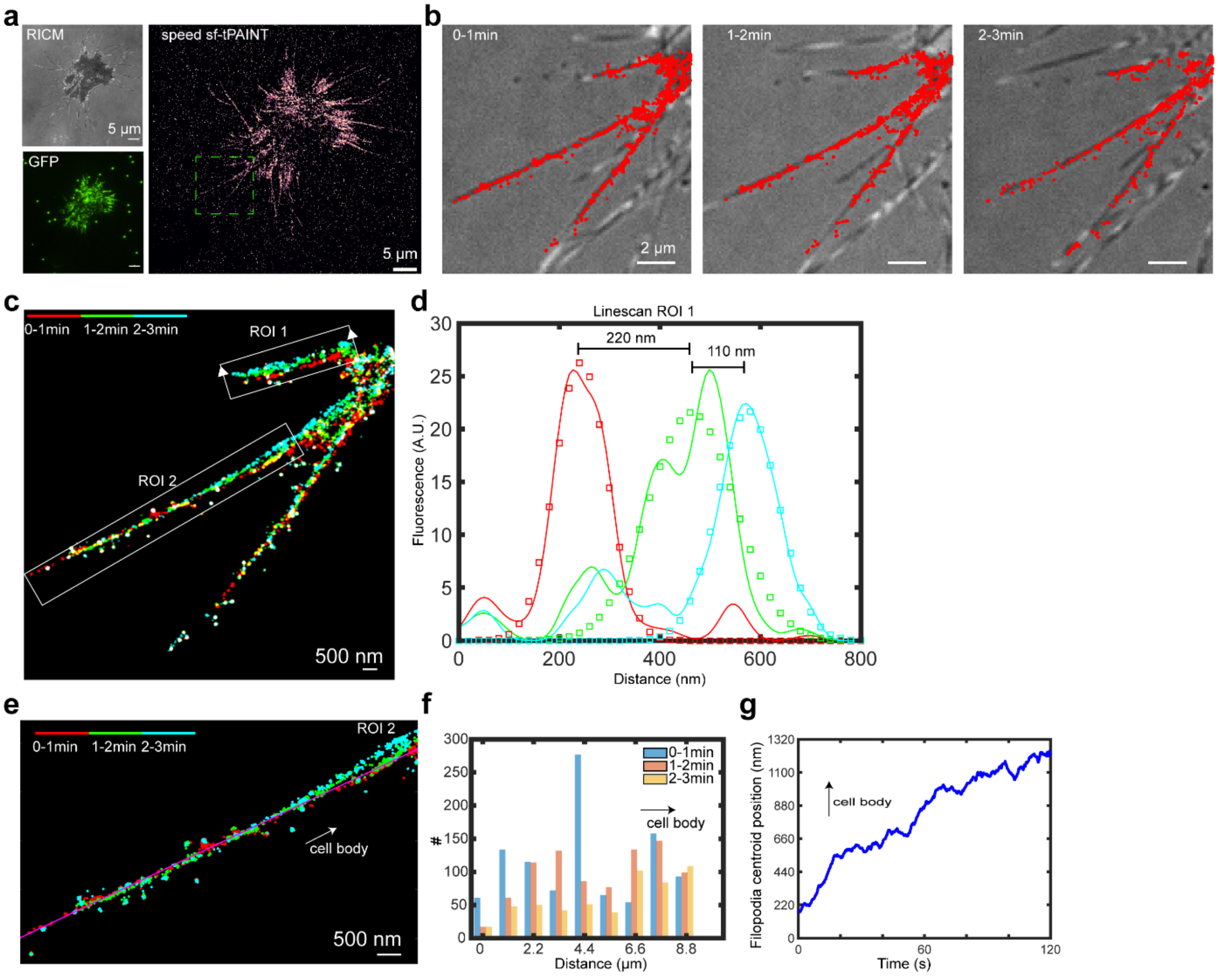

Supplementary Figure 7: sf-tPAINT mapping of dynamic filopodial forces (**a**) A subset of MEF GFP-vinculin cells produced filopodia after they spread on cRGD-presenting 9.1 pN tPAINT surfaces. Integrating 900 frames (collected at 5 Hz; 3 min total time imaging interval) revealed integrin-generated tension exerted by the fibroblast. (**b**) Filopodia were identified using RICM. Time-resolved single-molecule tension localizations were manually masked according to the contact area of individual filopodia. The region shown in (**b**) corresponds to the green box from (**a**). Note that only the localizations within the region of interest are displayed and analyzed in in **b-g**. (**c**) Overlay of sf-tPAINT filopodial tension dynamics. Color indicates the time bin during which the localizations were observed. (**d**) Linescans from the region indicated in the white box from **c** reveal lateral filopodial "scanning". Data points (squares) are derived from a Gaussian fit of the raw data which is represented by solid lines. (**e**) Zoom-in of middle filopodia from (**c**) where color indicates the time bin. The magenta line represents a best fit calculated using linear regression. (**f**) Histogram of single molecule localizations projected onto the magenta line from **e**. (**g**) Filopodial centroid position inferred from the average projection of single-molecule localizations onto the magenta line within a 1 min sliding window reveals the dynamics of filopodial retraction. Note that this data was collected via the speed-optimized tPAINT probe (**Extended Data Fig. 5**). 3 MEF-GFP vinculin fibroblasts from *n* = 2 independent experiments produced filopodial tension measurable via speed-optimized sf-tPAINT probes. The analyses presented in **c-g** were performed for one cell as a proof-of principle.

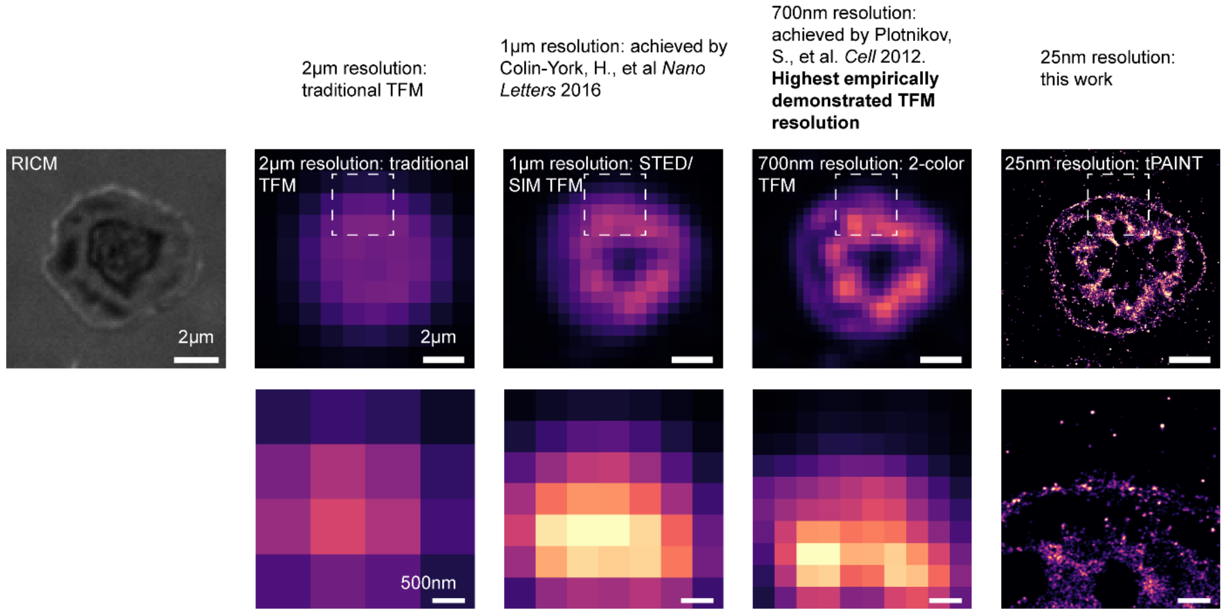

Supplementary Figure 8: Comparison of resolution between TFM and sf-tPAINT. (**a**) 8.5 pN sf-tPAINT images of platelet rendered at 2 μm, 1 μm, 0.7 μm, and 25 nm resolution. The 0.7 μm resolution represents the highest demonstrated resolution for TFM using two-color confocal imaging. Importantly, the edge tension of human platelets is only clearly resolved using sf-tPAINT.

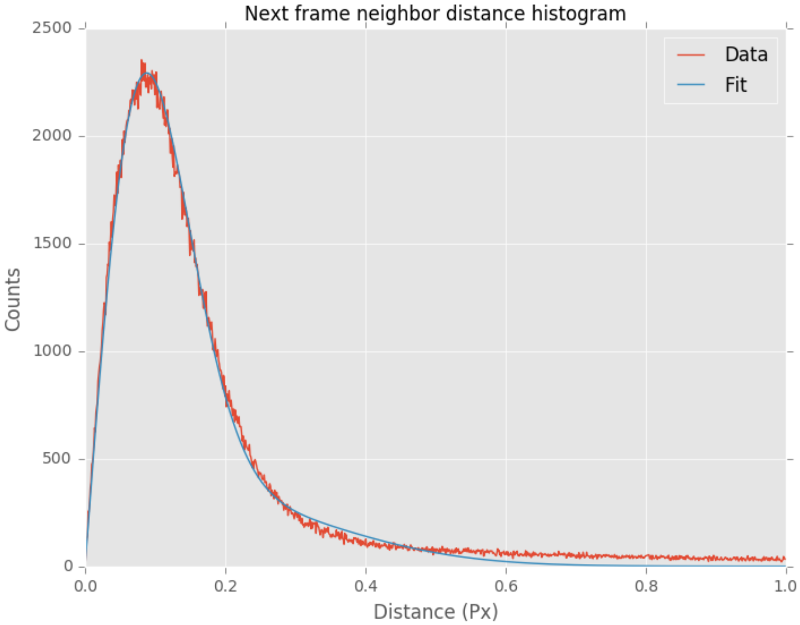

Supplementary Figure 9: Nearest-neighbor distance demonstrates ~10 nm precision in accumulated-tPAINT measurements. The nearest-neighbor localizations in temporally adjacent frames were calculated in Picasso to determine the localization precision as previously described[4]**.** For the single molecule localizations that produced the image in **Fig. 3b-f**, the nearest neighbor distance was calculated as 0.09 pixels, corresponding to a precision of ~10 nm.

Name	**Sequence (5’ to 3’)**
Imager	CTAGATGTAT/3AmMO/
Imager with Cy3B	CTAGATGTAT/3Cy3B/
Imager with Atto488	CTAGATGTAT/3Atto488/
Speed imager	TCCTCCC/3AmMO/
Speed imager with Cy3B	TCCTCCC/3Cy3B/
Imager-moderate/high	TAA TGA AGA/3AmMo/
Imager-moderate/high with Cy3B	TAA TGA AGA/3Cy3B/
Accumulated-tPAINT ligand with BHQ2	TAGATGTAT/iBHQ-2/GAGGCACGACAC/35OctdU/
Accumulated-tPAINT anchor	/5Biosg/GTGTCGTGCCT/iUniAmM/CATACATCTA
Strain-free tPAINT backbone	GTGAAATACCGCACAGATGCGTTTTTTTTTTTT TTTTTTTTTTTTTTTTTTTA AGAGCGCCACGTA GCCCAGC
Strain-free tPAINT anchor with BHQ2	/5BHQ_2/GTAGATGTATCTTTCGCATCTGTGCG GTATTTCAC/3Bio/
Strain-free tPAINT ligand	/55OctdU/GCTGGGCTACGTGGCGCTCTTTTTG ATACATCTAC/3AmMO/
Strain-free tPAINT ligand with Cy3B	/55OctdU/GCTGGGCTACGTGGCGCTCTTTTTG ATACATCTAC/3Cy3B/
Strain-free tPAINT ligand_moderate	/55OctdU/GCTGGGCTACGTGGCGCTCTTTTTG TCTTCATTAGTGCTC/3AmMo/
Strain-free tPAINT anchor_moderate with BHQ2	/5BHQ_2/GAGCACTAATGAAGACTTTCGCATCT GTGCGGTATTTCAC/3Bio/
Strain-free tPAINT ligand_high	/55OctdU/GCTGGGCTACGTGGCGCTCTTTTTG TCTTCATTACTGTCGTGCCTC/3AmMO/
Strain-free tPAINT anchor_high with BHQ2	/5BHQ_2/GAGGCACGACAGTAATGAAGACTTT CGCATCTGTGCGGTATTTCAC/3Bio/
Strained-tPAINT backbone	GTGAAATACCGCACAGATGCGTTGTAGATGTA TTTTTTTTATACATCTACTTAAGAGCGCCACGTAGCCCAGC
Strained-tPAINT anchor	CGCATCTGTGCGGTATTTCAC/3Bio/
Strained-tPAINT anchor with BHQ2	/5BHQ_2/CGCATCTGTGCGGTATTTCAC/3Bio/
Strained-tPAINT ligand	/55OctdU/GCTGGGCTACGTGGCGCTCTT/3AmMO/
Strained-tPAINT ligand with Cy3B	/55OctdU/GCTGGGCTACGTGGCGCTCTT/3Cy3B/
Speed tPAINT v1 ligand	/55OctdU/GCTGGGCTACGTGGCGCTCTTGGGAGGA
Speed tPAINT v1 anchor	TCCTCCCCGCATCTGTGCGGTATTTCAC/3Bio/
Speed tPAINT v2 ligand	/55OctdU/GCTGGGCTACGTGGCGCTCTTGGGAGGAG
Speed tPAINT v2 anchor	CTCCTCCCCGCATCTGTGCGGTATTTCAC/3Bio/
Speed tPAINT v3 ligand	/55OctdU/GCTGGGCTACGTGGCGCTCTTGGGGAGGAG
Speed tPAINT v3 anchor	CTCCTCCCCCGCATCTGTGCGGTATTTCAC /3Bio/
Speed tPAINT v3_control ligand	/55OctdU/GCTGGGCTACGTGGCGCTCTTTTTCGGGAGGAC
Speed tPAINT v3_control anchor	GTCCTCCCGTTTCGCATCTGTGCGGTATTTCAC/3Bio/
Speed tPAINT v3_spacer ligand	/55OctdU/GCTGGGCTACGTGGCGCTCTTTTTGGGGAGGAG
Speed tPAINT v3_spacer anchor	CTCCTCCCCTTTCGCATCTGTGCGGTATTTCAC/3Bio/

Supplementary Table 1: Oligonucleotide Sequences. Sequences used in this work are listed above. /5Biosg/ = biotin ligated to the 5’ terminus. 3Bio = biotin ligated to the 3’ terminus. 3AmMO = amine linked to the 3’ DNA terminus. 5OctdU = 5’ terminal alkyne. 3BHQ 2 = Black Hole Quencher 2 attached to the 3’ DNA terminus. 3Cy3B = Cy3B attached to the 3’ DNA terminus.

Product	Retention time (Minutes)
Imager	5.8
Imager with Cy3B	14.9
Speed imager	5.8
Speed imager with Cy3B	15.5
Accumulated-tPAINT ligand with BHQ2	15.9
Accumulated-tPAINT ligand with BHQ2 - c(RGDfK(PEG-PEG))	18.3
Strain-free tPAINT ligand	15.3
Strain-free tPAINT ligand - c(RGDfK(PEG-PEG))	17.8
Strained-tPAINT ligand	12.1
Strained-tPAINT ligand - c(RGDfK(PEG-PEG))	15.7
Speed tPAINT ligand v1	15.5
Speed tPAINT ligand v1 - c(RGDfK(PEG-PEG))	18.9
Speed tPAINT ligand v2	14.9
Speed tPAINT ligand v2 - c(RGDfK(PEG-PEG))	18.5
Speed tPAINT ligand v3	15.9
Speed tPAINT ligand v3 - c(RGDfK(PEG-PEG))	17.9
Speed tPAINT ligand v3_control	15.4
Speed tPAINT ligand v3_control - c(RGDfK(PEG-PEG))	18.6
Speed tPAINT ligand v3_spacer	16.0
Speed tPAINT ligand v3_spacer - c(RGDfK(PEG-PEG))	18.2

Supplementary Table 2: Retention time on HPLC of oligonucleotides.

Setting	Condition
Microscope	Nikon Ti
Gain camera channel 561	EM gain: 300
Field of view	512 x 512 pixel
Exposure time	200 ms
Binning	No binning
Excitation laser	561 (max power = 75 mW) 488 (max power = 80 mW)
MEF Accumulated-tPAINT	
Laser power	30 %
Imaging buffer	FluoroBrite
Imager concentration	2.5 nM
Mg^{2+} concentration	Figure 3, Extended Data Figure 2: 0.8 mM
MEF Strain-free tPAINT	
Laser power	20 %
Imaging buffer	FluoroBrite
Imager concentration	10 nM
Mg^{2+} concentration	Extended Data Figure 2, Figure S4: 0.8 mM Figure 1, S3, S6, Extended Data Figure 2, 4: 75 mM
MEF Speed-optimized tPAINT	
Laser power	20 %
Imaging buffer	FluoroBrite
Imager concentration	10 nM
Mg^{2+} concentration	Extended Data Figure 5: 0.8 mM Extended Data Figure 5, Figure S7: 75 mM
Platelet Accumulated-tPAINT	
Laser power	30 %
Imaging buffer	Tyrode's buffer
Imager concentration	2.5 nM
Mg^{2+} concentration	Figure 3, Extended Data Figure 2, 3: 2 mM
Platelet Strain-free tPAINT	
Laser power	30 %
Imaging buffer	Tyrode's buffer
Imager concentration	10 nM
Mg^{2+} concentration	Figure,, S4, Extended Data Figure 1, 2, 3, 7: 2 mM Figure 1, S5, S8, Extended Data Figure 3, 4, 8, 10 : 37.5 mM
Platelet strained tPAINT	
Laser power	30 %
Imaging buffer	Tyrode's buffer
Imager concentration	10 nM
Mg^{2+} concentration	Extended Data Figure 1: 2 mM
Platelet Exchange-tPAINT	
Laser power	30 %
Imaging buffer	Tyrode's buffer
Imager concentration	7.5 nM (tension); 1 nM (F-actin)
Mg^{2+} concentration	Figure 2: 37.5mM (tension), 2 mM (F-actin)
Platelet force-multiplexed tPAINT	
Laser power	488 nm: 60 %; 561 nm: 40%

Imaging buffer	Tyrode’s buffer
Imager concentration	7.5 nM
Mg^{2+} concentration	Figure 2: 37.5 mM
DNA Origami DNA PAINT	
Laser power	30 %
Imaging buffer	5 mM Tris-HCl, 5 mM NaCl, 10 mM $MgCl_2$ and 1 mM EDTA at pH 8.0
Imager concentration	2.5 nM

Supplementary Table 3: Imaging conditions in this work. Laser power is given as percent of the maximum power, defined in the Nikon Elements GUI.

	Year	Spatial resolution	Bead density	Bead size	Required microscope	Note
Sabass et al., *Biophysical Journal*[5]	2008	1 µm	N/A	40 nm	Confocal	Two color beads
Plotnikov, S., et al., *Cell*[6]	2012	0.7 µm	N/A	40 nm	Confocal	Two color beads
Colin-York et al. *Nano Letters*[7]	2016	1-1.2 µm	2.2 /µm^2	40 nm	STED, Confocal	Modeling suggests 500 nm is possible with 15 beads/µm^2, this resolution is not demonstrated
Polacheck, W., and Chen, C. *Nature Methods*[8]	2016	2 µm for 2D 5 µm for 3D	N/A	N/A	Confocal microscope	Review article of the existing techniques
Colin-York et a. *Nano Letters*[9]	2019	1 µm	1 /µm^2	100 nm	SIM	Modeling suggests 500 nm is possible with 15 beads/µm^2, this resolution is not demonstrated
Stubb, A., et al. *Nano Letters*[10]	2020	1-2 µm	1.2 /µm^2	40 nm	Spinning-disk confocal or widefield microscope	Fourier ring correlation for beads tracking with 40 nm spatial resolution, no resolution is indicated for traction reconstruction
Tension PAINT (this study)	2020	25 nm	None	None	Standard fluorescence microscope	

Supplementary Table 4: Summary of resolution achieved in state-of-the-art traction force microscopy (TFM) methods.

Supplementary Note 1: Probe design considerations

One of the most sensitive techniques for measuring receptor forces is DNA-based molecular tension probes. These probes act as force-triggered switches, and are generally comprised of a force-extensible element (e.g. a polymer/protein chain, or a DNA stem-loop structure) flanked by a fluorophore-quencher pair[11-14]. When receptor forces are transmitted to the molecular tension probe, the force-extensible element extends, separating the fluorophore from the quencher and producing an up to 100x increase in fluorescence[15]. Examples of the fluorescence data from turn-on DNA tension probes are provided in **Extended Data Fig.1e-f**, and **Supplementary Fig. 3**.

Challenges in adapting turn-on tension probes for super-resolution imaging

Many challenges complicate the use of turn-on tension probes for sub 100-nm super resolved imaging of receptor mechanics. Quenching processes, such as the Cy3B-BHQ2 quenching that provides contrast in **Extended Data Fig.1** and **Supplementary Fig. 3** are challenging to integrate with stochastic super resolution microscopy techniques such as STORM. To our knowledge, FRET indexes have never been successfully calculated for fluorophores via stochastic super-resolution imaging techniques because both the donor and acceptor would have to simultaneously be in the excitable (ON) state. Attempts to integrate single-molecule FRET with STED are ongoing[16, 17]; however, STED requires specialized optics and the most sensitive molecular tension probes on dark quenchers (e.g. BHQ2) not fluorescent donor-acceptor FRET pairs[13, 15].

Fluorophore-quencher pairs are also challenging to adapt for use with many super-resolution imaging modalities. For example, quenching Cy5 with BHQ2 produces photoswitching[18]. In the context of tension probes where fluorescence intensity reports receptor tension, photoswitching of the fluorophore would produce spurious, non-mechanical single molecule localizations. Additionally, both the fluorophore and quencher may photobleach[19], leading to a failure to report pN forces or to spurious, non-mechanical fluorescence events, respectively. Finally, in dSTORM, a small subset of fluorophores are activated within each cycle. These fluorophores may not coincide with the subpopulation of tension probes experiencing mechanical force, leading to low localization density. The data from this work demonstrate the critical importance of rapid sampling of mechanically unfolded probes and high localization density to achieve sub-100 nm spatial resolution (**Extended Data Fig.3, Extended Data Fig. 5**). In summary, it is unlikely that techniques such as dSTORM could be applied to measure pN receptor forces via turn-on tension probes. STED may offer a route to rapid, turn-on tension measurement, but requires specialized optics and is subject to photobleaching. DNA-PAINT circumvents these issues. It is robust to photobleaching and requires only one fluorophore, avoiding the challenges associated with FRET and quencher-induced photoswitching. The principal challenge for DNA-PAINT is achieving rapid imager sampling to quantify receptor forces.

Design of DNA-PAINT tension probes

To adapt DNA tension probes for super-resolved imaging of receptor mechanics, we leveraged the technique DNA-Points Accumulation for Imaging in Nanoscale Topography (DNA-PAINT). DNA-PAINT relies on the transient binding of fluorophore-tagged “imager” strands to ssDNA “docking” sequences decorating the biomolecule of interest[20, 21]. We reasoned that when pN receptor forces open the stem structure of DNA-based molecular tension probes, the stem opening exposes ssDNA to solution that was previously concealed. Therefore, if a DNA-PAINT docking site is concealed within the stem DNA-based tension probe, the probe can function as a force-triggered switch that only permits imager binding when the probe is experiencing pN receptor forces exceeding the probe $F_{1/2}$ (**Fig. 1a**).

However, these probes must be designed carefully. Mechanical forces exerted on DNA can stretch ssDNA beyond its equilibrium, zero force length. This overstretching can reduce the on rate of imager hybridization when the docking site is experiencing pN mechanical force[22]. Therefore, we suspected that imagers would have a reduced binding rate to conventional DNA tension probes in which the cryptic docking site is encoded in the mechanically strained stem-loop structure (**Fig. 1b**). To confirm this hypothesis, we constructed a kinetic model which confirmed that larger, ~10 pN magnitudes of *F* impede the kinetics of DNA-DNA binding (**Supplementary Note 2, Extended Data Fig.1**). To support this model's predictions, we empirically demonstrated that imager binding to tension probes under the influence of receptor-generated forces is impeded (**Extended Data Fig.1**).

To overcome this obstacle, we moved the imaging docking site away from the conventional stem-loop. Before probe opening, receptor forces are borne by a DNA stem structure that conceals the cryptic docking site (**Fig. 1a**); however, upon probe opening under pN receptor forces, the redesigned "strain-free" tPAINT probe funnels force away from the docking site, allowing imagers to bind to an non-mechanically strained docking site (**Fig. 1a, b**). This redesign lowers the energy barrier to imager binding to mechanically-opened sf-tPAINT probes, allowing imagers to bind regardless of the magnitude of the receptor force (**Fig. 1a**, **Extended Data Fig.1**).

In tPAINT, it is critical to balance the mechanical barrier to probe opening ($F_{1/2}$) with the thermal stability of the tension probe. If the probe $F_{1/2}$ is too high, receptor forces fail to frequently unfold the probe, thus very few single molecule localizations will be observed. In contrast, if the thermal stability (and mechanical stability) is set too low, probes will open spontaneously, producing spurious non-mechanical single molecule localizations. Work by Woodside and colleagues suggests that incorporating GC bases at the termini of the stem structure will stabilize the folded state of the stem and accelerate refolding rate[23]. Therefore, engineering GC bases at the termini in tPAINT probes is advantageous as it will reduce the spontaneous hairpin breathing and background tPAINT signal. Accordingly, we incorporated GC base pairs flanking the docking site to increase the stability of the probe and suppress background imager binding.

Finally, we adjusted the stem-loop length of the tPAINT probe (31 T bases) to match the contour length of the previously reported MTFM hairpin probe that also contained 31 bases[13]. The redesigned strain-free tPAINT probe thus has a 31 T "backbone," and a 13.2 nm extension under force (using $x = 0.44(n-1)$ nm, where *n* represent the number of the bases comprising the stem-loop of hairpin). The 13.2 nm hairpin extension is more than twice the quenching distance of Cy3B-BHQ2 allowing us to synthesize turn-on variants of the sf-tPAINT probe and to conduct widefield fluorescence measurements of receptor tension to validate the function of the probe (**Extended Data Fig. 1, Supplementary Fig. 3**).

To determine the $F_{1/2}$ of the sf-tPAINT probe, we utilized the worm-like chain model and previously published calculations[13]. Briefly, the $F_{1/2}$ is calculated as:

$$F_{1/2} = \frac{\Delta G_{fold} + \Delta G_{stretch}}{\Delta x} \tag{1}$$

	$\Delta G_{stretch}$ (kJ/mol)	ΔG_{fold} (kJ/mol)	$F_{1/2}$ (pN)
MTFM probe	21.63	26.73	7.17
Strained tPAINT probe (No Mg^{2+})	21.63	27.07	7.22
Strained tPAINT probe	21.63	34.14	8.27
Strain-free tPAINT probe (No Mg^{2+})	21.63	27.82	7.33
Strain-free tPAINT probe	21.63	35.60	8.49
Speed-optimized tPAINT probe v1	21.63	24.77	6.87
Speed-optimized tPAINT probe v2	21.63	30.63	7.75
Speed-optimized tPAINT probe v3	21.63	39.2	9.02

Speed-optimized tPAINT probe v3_control	21.63	41.80	9.4
Speed-optimized tPAINT probe v3_spacer	21.63	38.45	8.91
Strain-free tPAINT probe_moderate	21.63	74.68	14.28
Strain-free tPAINT probe_high	21.63	121.21	21.18

Supplementary Note 1, Table 1: Calculated probe $F_{1/2}$

ΔG_{fold} is acquired from the IDT oligoanalyzer 3.1, which uses the UNAfold software package. The ΔG_{fold} was calculated using 140 mM monovalent and 37.5 mM divalent salt at 25 °C and at a concentration of 250 nM oligonucleotide. $\Delta G_{stretch}$ is calculated using following equation a:

$$\Delta G_{stretch} = \frac{k_B T}{L_p} \frac{L_c}{4(1-x/L_c)} \left[3\left(\frac{x}{L_c}\right)^2 - 2\left(\frac{x}{L_c}\right)^3\right] \qquad (2)$$

Parameter	Definition	Value
T	Temperature	298 K (25°C)
k_B	Boltzmann constant	1.380648e-23 kJ/K
n	Number of nucleotides in loop	31
x	Loop extension	0.44(n-1) nm
Δx = x-2	Loop displacement	(0.44(n-1)-2) nm
L_c	Contour length	0.63 nm per nucleotide
L_p	Persistence length ssDNA	1.3 nm

Supplementary Note 1, Table 2: Parameters for probe $F_{1/2}$ calculations.

Supplementary Note 2: Imager binding kinetics to mechanically strained docking sites

When tension (F) is applied to single stranded DNA, larger magnitudes of F ($F > 10$ pN for our probes) impose a kinetic barrier to hybridization to its complement (e.g. the imager)[24]. Similarly, F applied to a duplex will increase its dissociation rate[24]. Accordingly, receptor tension that acts to unfold a DNA stem-loop tension probe (strained-tPAINT) will impede imager hybridization to the cryptic docking site. The barrier to hybridization will also increase as a function of the magnitude of applied F. The strain-free tPAINT (sf-tPAINT) probe described in this work is designed to avoid this issue. The sf-tPAINT probe presents a non-mechanically strained docking site which is available for imager binding in a force-independent manner. To develop a quantitative understanding for the force-dependence of imager binding to the two probe constructs (conventional[13] strained-tension probe compared to the sf-tPAINT probe), we adapt the force-dependent hybridization kinetics and dehybridization models from Woodside & Block *et. al.*[23], and Whitley, Comstock, & Chemla[24]. Specifically, we use these models to estimate the barrier for imager binding as a function of applied F. This is a critical parameter as it dictates the frequency of localizations and the temporal resolution of live-cell tPAINT.

Model Overview: We define three discrete chemical states of a tension probe, as shown in **Extended Data Fig.1a**: closed, opened, and imager-bound (hereafter simply called "bound"). These three states are considered for the conventional strained tension probes as well as the sf-tPAINT probes. For both types of probes, the transition between the closed and opened states (step **1** in **Extended Data Fig.1a**) is force-dependent (**Extended Data Fig.1b**). However, the two probes diverge in the force-dependence of imager binding (step **2** versus step **3** in **Extended Data Fig.1a**). To consider the force-dependence of each probe, we constructed a model of the tPAINT-imager system. We first consider the kinetics for the transition between the closed and open states. Then we incorporate the imager binding kinetics as a function of force. These kinetic equations are then used to infer the equilibrium distribution of tPAINT probes in the three states.

Model construction – force-dependent hairpin kinetics: To calculate the F-dependent equilibrium distribution of these states, we first calculate the kinetic rate constants of each of the four possible transitions as a function of F (k_{open}, k_{close}, k_{off}, and k_{on} – see **Extended Data Fig.1a**). We model the first three constants as zero-order rate constants that strictly depend on F (for given imager and hairpin sequences), and k_{on} is a pseudo-first-order rate constant such that imager binding also depends on the concentration of the imager, C.

The zeroth-order rate constant for hairpin opening, k_{open}, can be approximated using the Bell model[25] as discussed in Woodside & Block *et al.*[23] according to the equation:

$$k_{open}(F) = k_{open}(0)\exp\left(\frac{F\Delta x_f^{\ddagger}}{\mathrm{k_B T}}\right) \tag{1}$$

where $k_B T = 4.114$ pN nm is the Boltzmann constant at room temperature, $k_{open}(0)$ is the zero-force opening rate, and $\Delta x_f^{\ddagger}$ is the force-independent extension from the folded state to the transition state. We used $\Delta x_f^{\ddagger} = 5.1\, nm$ and $k_{open}(0) = 0.017 s^{-1}$ based on experimentally-measured parameters for the "10R50/T4" hairpin studied in Woodside *et al.*, which had a 10 base pair (bp) stem of 50% GC content (similar to the strained tPAINT probe in this work) and a 4 nucleotide (nt) loop (values presented in figure 3 and table 1 of ref. [23]). While the 4 nt loop in the 10R50/T4 hairpin is smaller than the 7 nt loop used in our strained tPAINT probe, the same study showed that $\Delta x_f^{\ddagger}$ and $k_{open}(0)$ do not depend meaningfully on loop size[23]. Also note that these values were determined in 50 mM MOPS and 200 mM KCl buffer at room temperature.

The zeroth-order rate constant for hairpin closing, $\mathrm{k_{close}}$, can be approximated using a similar form:

$$k_{close}(F) = k_{close}(0)\exp\left(-\frac{F\Delta x_u^{\ddagger}}{k_B T}\right) \tag{3}$$

where $\Delta x_u^{\ddagger}$ is the force-independent change in distance between the unfolded state and the transition state for hairpin closing and $k_{close}(0)$ is the zero-force hairpin closing rate. The $\Delta x_u^{\ddagger}$ reported for the 10R50/T4 hairpin by Woodside *et. al* was 4.0 nm, but that study found that $\Delta x_u^{\ddagger}$ depends strongly on loop and stem length. While a construct with a 10 bp stem and a 7 nt loop was not studied, hairpins with 15 bp stems with loops ranging in length from 3 nt to 20 nt were studied, and a linear trend between loop length and $\Delta x_u^{\ddagger}$ was observed. We found through curve fitting that the slope of that trend was 0.4 nm/nt, and so we adjusted their reported $\Delta x_u^{\ddagger}$ value to obtain $\Delta x_u^{\ddagger} = 4.0\,nm + (3\,nt)(0.4\,nm/nt) = 5.2\,nm$. We solved for $\mathrm{k}_{close}(0)$ by setting $F_{1/2} = 8\,\mathrm{pN}$ and setting $k_{open}(F_{1/2}) = k_{close}(F_{1/2})$:

$$k_{close}(0)\exp\left(-\frac{8\,pN\;5.2\,nm}{4.114\,pN\,nm}\right) = k_{open}(0)\exp\left(\frac{8\,pN\;5.1\,nm}{4.114\,pN\,nm}\right) \tag{4}$$

$$k_{close}(0) = k_{open}(0)\exp\left(\frac{8\,pN}{4.114\,pN\,nm}(5.1\,nm + 5.2\,nm)\right) \tag{5}$$

$$k_{close}(0) = 8.3 * 10^{6}\,s^{-1} \tag{6}.$$

<u>*Model validation – F-dependent hairpin kinetics:*</u> Before considering the kinetics of image hybridization, we first validated that the F-dependence of hairpin opening could be accurately reconstructed from the mathematical relationships presented above. We constructed a Markov matrix (M) to represent state transitions and solved for the steady state fraction of probes in an open state (χ_o) and a closed state (χ_c) at a given force magnitude with the assumption that all probes were initially in a closed state:

$$\begin{bmatrix}\chi_c\\ \chi_o\end{bmatrix} = \mathrm{M}^{\mathrm{p}}\begin{bmatrix}1\\0\end{bmatrix} = \begin{bmatrix}1-\Delta t k_{open} & \Delta t k_{close}\\ \Delta t k_{open} & 1-\Delta t k_{close}\end{bmatrix}^{\mathrm{p}}\begin{bmatrix}1\\0\end{bmatrix} \tag{7}$$

where $\Delta\mathrm{t}$ is the duration of simulation timestep and p is a positive integer representing the number of simulation timesteps. In order to ensure stability of the dynamic system, we selected a small timestep ($\Delta\mathrm{t} = 10^{-9}\,\mathrm{s}$). To best approximate equilibrium conditions, we also simulated a very large number of timesteps ($\mathrm{p} = 10^{10}$), yielding an equilibration time of $10\,\mathrm{s}$, which is larger than an order of magnitude than the timescale of imager binding. We found that in the absence of imager we had a typical χ_o vs. F profile (not shown), wherein χ_o increases from ~0 to ~1 over a range of forces that spans 4 pN that is centered on the $8\,\mathrm{pN}$ $F_{1/2}$.

<u>*Model construction – force-dependent imager binding kinetics:*</u> We next consider the kinetics of imager binding and unbinding. For unbinding, k_{off} is described using an adaptation of the Bell Model developed by Whitley, Comstock, and Chemla [24]:

$$k_{off}(F) = k_1\exp\left(-\frac{\Delta G^{\ddagger}(F)}{k_B T}\right) = k_1\exp\left(-\frac{\Delta G^{\ddagger}(0) - \int_0^F\left(x^{\ddagger}(f) - x_b(f)\right)df}{k_B T}\right) \tag{8}$$

where k_1 is the unbinding attempt rate, $\Delta G^{\ddagger}(0)$ is the zero-force activation energy barrier height, f is an integration variable, and $x^{\ddagger}(\mathrm{f})$ and $x_b(\mathrm{f})$ are the force-dependent extensions of the transition state and bound state, respectively. Here, we use $k_1 = 10^{7}\,s^{-1}$ according to literature precedent[24]. We also analyzed supplemental figure 7 of ref. [24] and found that $\Delta G^{\ddagger}(0)$ could be approximated by the relation $\Delta G^{\ddagger}(0) = 0.45 + (1.65 \times Duplex\ length)$ (in units of $k_B T$) for duplexes 8-10 bp in length, thus yielding $\Delta G^{\ddagger}(0) = 15.3\ k_B T$. This value yields $k_{off}(0) = 0.23\ s^{-1}$, which is within an order of magnitude of the imager unbinding rate measured in our work despite the differing buffer conditions. Both $x^{\ddagger}(\mathrm{f})$ and $x_b(\mathrm{f})$ can be calculated using the worm-like-chain (WLC) model, which describes the relationship between the entropic tensile force of a polymer chain and the chain's end-to-end extension. This relationship can be accurately approximated using the numerical approximation developed by Petrosyan[26]:

$$x_{WLC} = bN\left(\frac{4}{3} + \frac{4}{3\sqrt{\frac{FP}{k_BT}} + 1} - \frac{10\exp\left(\sqrt[4]{900\frac{k_BT}{FP}}\right)}{\sqrt{\frac{FP}{k_BT}}\left(\exp\left(\sqrt[4]{900\frac{k_BT}{FP}}\right) - 1\right)^2} + \frac{\left(\frac{FP}{k_BT}\right)^{1.62}}{3.55 + 3.8\left(\frac{FP}{k_BT}\right)^{2.2}}\right) \qquad (9)$$

where b is the polymer's length per monomer (in nm), N is the number of monomers in the segment (for nucleic acids, segment length is measured in basepairs or nucleotides) and P is the persistence length of the polymer. For the calculation of $x_b(\mathrm{f})$ we used $b = 0.34\ \mathrm{nm}$ and $P = 53\ nm$, as was used by Whitley *et al.*[24] For the calculation of $x^{\ddagger}(\mathrm{f})$ we used $b = 0.54\ nm$ and $P = 2.6\ nm$, as calculated by Whitley *et al.*[24] For both we used $N = 9$, which corresponds to the length of the imager. Finally, a similar equation can be used to calculate k_{on} as a function of *F:*

$$k_{on}(F) = k_1 \exp\left(-\frac{\left(\Delta G^{\ddagger}(F) - \Delta G^{o}(0) + \int_0^F \left(x_u(f) - x_b(f)\right)df\right)}{k_BT}\right) \qquad (10)$$

ΔG^{o} is the free energy of hybridization and $x_u(f)$ is the force-dependent extension of the unbound imager docking site and can be calculated from equation (10) with $P = 53\ nm$ and $b = 0.34\ nm$. (Note: equation 10 was obtain by modifying equation 5 in ref. [24]. We were unable to use equation 5 in ref. [24] to reproduce results resembling those presented in the work until we modified the equation from "$\Delta G^{o}(F) + \Delta G^{\ddagger}(F)$" to "$-\Delta G^{o}(F) + \Delta G^{\ddagger}(F)$". Equation 10 above is a rearranged form of this modified version of the equation from ref. [24]). As with our estimate of $\Delta G^{\ddagger}(0)$, we estimated $\Delta G^{o}(0)$ by analyzing supplemental figure 7 from ref. [24] and found that $\Delta G^{\ddagger}(0) = 2.45 + (1.65 \times Duplex\ Length)$, yielding $\Delta G^{o}(0) \approx 17.3\ k_BT$ and, as such, $k_{on}(0) = 7.4 * 10^{6}\ M^{-1}\ s^{-1}$ (which is consistent with literature estimates[24]).

Using these parameters, we constructed a new Markov-matrix equation to simulate the steady state dynamics in the presence of an imager, wherein probes can also reversibly transition from an open state to a bound state denoted by χ_b.

$$\begin{bmatrix}\chi_c\\ \chi_o\\ \chi_b\end{bmatrix} = \begin{bmatrix}1 - \Delta t k_{open} & \Delta t k_{close} & 0\\ \Delta t k_{open} & 1 - \Delta t(k_{close} + k_{on}C) & \Delta t k_{off}\\ 0 & \Delta t k_{on}C & 1 - \Delta t k_{off}\end{bmatrix}^{\mathrm{p}} \begin{bmatrix}1\\ 0\\ 0\end{bmatrix} \qquad (11)$$

We also note that the relationships for k_{on} and k_{off} are only relevant to conventional DNA hairpin tension probes, wherein the imager binding site is stressed. However, our new design has an unstressed imager binding site. As such, for our new design k_{on} and k_{off} are both force-independent constants. In other words, $k_{on}(F) = k_{on}(0)$ and $k_{off}(F) = k_{off}(0)$ for all F. For both cases, we can also measure the overall free energy of each of the three states:

$$\begin{bmatrix}E_c\\ E_o\\ E_b\end{bmatrix} = (\exp(\chi_c) + \exp(\chi_o) + \exp(\chi_b))^{-1} \begin{bmatrix}exp(\chi_c)\\ exp(\chi_o)\\ exp(\chi_b)\end{bmatrix} \qquad (12)$$

Model Results:

Applying equation 11 with the parameters described above, we were able to calculate the steady-state fractional probe occupancy of the bound (χ_b), open (χ_o), and closed (χ_c) states for a variety of F and C values. For the conventional/strained DNA hairpin probe with an imager concentration of $\mathrm{C} = 10\ \mathrm{nM}$, χ_{b} increases sharply as F approaches $F_{1/2}$ peaks at a value of ~27%, and then steadily decreases to zero as increasing F poses an increasing kinetic barrier to imager hybridization. These results are summarized in **Extended Data Fig.1c**. Integrin forces have been reported to range from 1-100pN (ref. [13, 14, 27]). At $F = 18\ \mathrm{pN}$, χ_b is 10-fold lower than its maximum value and equal to ~2.7%. In contrast, for the unstressed probe, χ_b increases monotonically as F increases above $F_{1/2}$ and then asymptotes to a value of 24.5%. To summarize, imager binding to the strained/conventional tPAINT probe is highly force-dependent within a physiologically-relevant force range, while binding to the new sf-tPAINT probe is not. Interestingly, χ_b for the strained-tPAINT probe peaks at a higher value than the χ_b asymptote for the sf-tPAINT probe (**Extended Data Fig.1c**) This counter-intuitive finding results from the fact that small magnitudes of force (<10 pN) actually increase the on-rate because this level of force helps to align the duplex in a linear manner which is thought to facilitate binding[24].

Note that, at the 10nM imager concentration, χ_b increases to a surprisingly high value of ~25%. This finding suggests that a large fraction of opened tension probes are bound at any given time. This observation is also illustrated by plots of $\mathrm{E_o}$, $\mathrm{E_c}$, and $\mathrm{E_b}$ as calculated with equation 12 (**Extended Data Fig.1c**). However, this observation may not be borne out experimentally because: 1) fluorophores may bleach before the imagers dehybridize, reducing the fraction of opened probes that result in fluorescent signal, 2) model parameters were estimated from literature values that were obtained under different buffer conditions to our experiments, and utilized different stem-loop sequences, and 3) our model assumes free diffusion of imagers beneath the cell whereas in reality the effective association rate of the imager to the probe may be impeded by the confined environment of the surface and particularly beneath the cell.

Supplementary Note 3: Experimental considerations for tPAINT measurements

Effects of imager sampling kinetics on tPAINT measurements

Many optical super-resolution microscopy measurements, including DNA-PAINT, rely on stochastic "blinking" of single molecules to resolve the spatial location of multiple fluorophores within a diffraction limited spot[20, 21, 28-31]. To produce a super-resolved image, the fluorophores localized within many consecutive imaging frames are combined to render a single super-resolved map. This integration over time presents a unique challenge to live-cell imaging because of cell dynamics and in our case force dynamics. In tPAINT, the sites of the probes are fixed, but each probe is transiently open and available for imager binding as long as $F > F_{1/2}$ which presents a unique challenge in live-cell tPAINT.

For example, the imager on rate is $k_{on} = 1.2\text{x}10^6\ M^{-1}s^{-1}$ for the traditional imager used in this study[21]. We independently validated this k_{on} by measuring its binding to a DNA-origami structure with a defined number of docking sites (**Extended Data Fig. 10**). For an imager concentration of 10nM, the expected influx rate of imager to an open cryptic docking site on a mechanically strained probe is 0.012 s^{-1}, meaning that, on average, an imager will visit an open sf-tPAINT probe once every 83.3 seconds. This slow sampling rate presents an issue because the lifetime of integrin-ligand bonds under force is ~0.1-20 sec[32, 33]. Because integrin-ligand bond lifetimes are significantly shorter than the 83 sec dark time in between imager binding events, tPAINT with conventional imager underestimates the number of binding events that occur. **Supplementary Fig. 4** depicts the real-time tPAINT images using the traditional imager sequence. However, the localization density remains low, likely due to the undersampling described above. Therefore, the events leading to cryptic docking site exposure are infrequently sampled. In principal, one could increase the influx rate of imager to the cryptic docking site to decrease the dark time. In practice, increasing the imager concentration produces more frequent sampling, but will increase the background in a concentration-dependent manner (**Extended Data Fig.6**) and is hence not a viable option in live-cell tPAINT.

An alternate route to increasing the quality of tPAINT images and reducing the undersampling of mechanically-opened tension probes is maximizing imager k_{on}. Indeed, we showed that increasing the value of k_{on} is critical for live cell imaging of dynamic mechanical events (compare **Fig.1** to **Supplementary Fig. 4**). The recently-developed speed-optimized PAINT strategy offers a method to maximize imager on-rate, thus better capturing short-lived mechanical events[34]. In speed-optimized PAINT, increasing [Mg^{2+}] from 10 mM to 75 mM produced a 2-fold increase in the influx rate. In our hands, the increase in localization number is even more dramatic because we perform experiments in cell culture media (DMEM) with [Mg^{2+}] of approximately 0.8 mM, or in Tyrode's solution with [Mg^{2+}] of 2 mM. Increasing the [Mg^{2+}] to 37.5mM during platelet experiments produced ~4-fold more localizations under the cell (**Fig. 1c, d and Extended Data Fig.3**, compare strain-free tPAINT to strain-free tPAINT with 37.5mM Mg^{2+}). Compare **Supplementary Fig. 4** with the platelet data from **Fig. 1c, d** to see the improvement offered by increasing imager k_{on}. Similar increases are produced for fibroblast integrin-generated tension.

Spurious, non-mechanical background signal in tPAINT measurements

To better understand the origin of background single molecule localizations outside the cell-surface contact area, we performed accumulated-tPAINT and sf-tPAINT with scrambled imagers. Sequence-scrambled Cy3B-labeled imagers produce up to a ~10-fold reduction in single molecule localizations compared to the specific imager (**Extended Data Fig.6**). This indicates that the majority of background localizations are driven by sequence specific binding to the docking site. This may be due to tPAINT probe thermal breathing as well as misfolded probes or probe impurities that lead to docking site exposure. Nonetheless, localization density is still 10 times greater under the cell compared to the background regions for sf-tPAINT, and 17 times greater than the background for accumulated-tPAINT (**Extended Data Fig .3**). This order-of-magnitude difference is due to mechanoselection whereby the majority of localizations are mechanically driven (**Extended Data Fig .3**).

Effect of [Mg^{2+}] on integrin traction forces

One potential issue associated with using elevated Mg^{2+} concentrations has to do with modulating cell biology. For example, the platelet integrin $\alpha_{IIb}\beta_3$ interacts with von-willebrand factor, fibrin, or fibrinogen during thrombus formation. The integrin $\alpha_{IIb}\beta_3$ interacts with a c-terminal γ-chain sequence (KQAGDV) of fibrinogen[35, 36] and also recognizes the Arg-Gly-Asp (RGD) sequence used in this work and in previous molecular tension probe experiments[37, 38]. The α_{IIb} subunit is made up of a small cytoplasmic region, TM domain, 2 "calf" domains, a "thigh" domain, and a C-terminal 7-bladed β-propeller. β_3 contains a larger cytoplasmic tail, TM domain, 4 EGF domains, a PSI domain, hybrid domain, and a β-I domain. According to structural models, integrins take on 3 main conformations with relation to ligand binding: a low affinity "bent" conformation, an intermediate affinity extended-closed conformation, and a ligand-bound high affinity state (extended with open headpiece).[39] Vital to integrin function are several binding sites for coordinating divalent cations, usually Ca^{2+} or Mg^{2+}. Formation of the dimeric integrin structure itself requires μM divalent cations, and both Ca^{2+} and Mg^{2+} can substitute for each other in some of the metal ion binding pockets.[40] The β_3 A-domain contains a metal ion dependent adhesion site (MIDAS), adjacent MIDAS (ADMIDAS), and synergistic metal binding site (SyMBS), where Mg^{2+} occupies the MIDAS and Ca^{2+} occupies the ADMIDAS and SyMBS.[41] The MIDAS Mg^{2+} coordinates the aspartate in the RGD, and in crystal structures of $\beta_{3,}$ the MIDAS is partially occupied at 1 mM Mg^{2+} and fully occupied at 5 mM Mg^{2+} concentrations[41]. Undoubtably, the use of 37.5mM Mg^{2+} during st-tPAINT platelet experiments will alter integrins behavior in these experiments.[41]

The effects of Mg^{2+} on platelet function have a long history in the literature, and likely have much to do with $\alpha_{IIb}\beta_3$. In the early 1990s, it was observed that low mM doses of Mg^{2+} prolonged bleeding time, and inhibited fibrinogen binding and aggregation of platelets[42], with aggregation being abolished in the 1-4 mM range[43]. Additionally, Mg^{2+} may inhibit other markers of platelet activation, such as P-selectin exposure[44, 45]. It is not immediately clear how to interpret the Mg^{2+} reliance of platelet integrins with the platelet inhibitory effect of similar concentrations of Mg^{2+}. β_3 contains two types of binding sites for metal ions, ligand competent (LC) sites which promote ligand binding, and inhibitory (I) sites which inhibit ligand binding by increasing the dissociation rate of RGD.[46] Initially the latter sites are a likely candidate for the effect of Mg^{2+}, but this hypothesis is weakened by these sites' Ca^{2+} specificity[47]. Nevertheless, it is possible that Mg^{2+} can "substitute" for Ca^{2+} here, especially at higher concentrations.

The effect of divalent cations is not limited to platelets. For example, Ca^{2+} and Mn^{2+} directly alter $\alpha_v\beta_3$ conformation[48]. Cations have been shown to alter the organization and formation of $\alpha_v\beta_3$ and $\alpha_v\beta_5$ focal adhesions[49]. It is reasonable to suspect that the 75 mM Mg^{2+}concentration employed in fibroblast experiments may also alter their biology.

In cases where live-cell force response is sensitive to Mg^{2+}, one can use sf-tPAINT without the high Mg^{2+} buffer (**Supplementary Fig. 4, Extended Data Fig .3**). Doing so preserves biological processes at the cost of lower localization frequency which can impact the spatial and temporal resolution of tPAINT. To ameliorate this issue, we designed a speed-optimized sf-tPAINT probe (**Supplementary Fig. 7**) which enables rapid imaging of forces at physiological [Mg^{2+}]. Additionally, live-cell accumulated-tPAINT can also be conducted at physiological [Mg^{2+}] with high localization frequency and high spatial resolution (**Fig. 3**).

References:

1. Gustafsson, N. *et al.* Fast live-cell conventional fluorophore nanoscopy with ImageJ through super-resolution radial fluctuations. *Nat Commun* **7**, 12471 (2016).
2. Morimatsu, M., Mekhdjian, A.H., Chang, A.C., Tan, S.J. & Dunn, A.R. Visualizing the interior architecture of focal adhesions with high-resolution traction maps. *Nano Lett* **15**, 2220-2228 (2015).
3. Liu, Y. *et al.* Nanoparticle tension probes patterned at the nanoscale: impact of integrin clustering on force transmission. *Nano Lett.* **14**, 5539-5546 (2014).
4. Endesfelder, U., Malkusch, S., Fricke, F. & Heilemann, M. A simple method to estimate the average localization precision of a single-molecule localization microscopy experiment. *Histochem Cell Biol* **141**, 629-638 (2014).
5. Sabass, B., Gardel, M.L., Waterman, C.M. & Schwarz, U.S. High resolution traction force microscopy based on experimental and computational advances. *Biophysical Journal* **94**, 207-220 (2008).
6. Plotnikov, S.V., Pasapera, A.M., Sabass, B. & Waterman, C.M. Force fluctuations within focal adhesions mediate ECM-rigidity sensing to guide directed cell migration. *Cell* **151**, 1513-1527 (2012).
7. Colin-York, H. *et al.* Super-Resolved Traction Force Microscopy (STFM). *Nano Letters* **16**, 2633-2638 (2016).
8. Polacheck, W.J. & Chen, C.S. Measuring cell-generated forces: a guide to the available tools. *Nat Methods* **13**, 415-423 (2016).
9. Colin-York, H. *et al.* Spatiotemporally Super-Resolved Volumetric Traction Force Microscopy. *Nano Lett* **19**, 4427-4434 (2019).
10. Stubb, A. *et al.* Fluctuation-Based Super-Resolution Traction Force Microscopy. *Nano Lett* (2020).
11. Ma, V.P. & Salaita, K. DNA Nanotechnology as an Emerging Tool to Study Mechanotransduction in Living Systems. *Small*, e1900961 (2019).
12. Stabley, D.R., Jurchenko, C., Marshall, S.S. & Salaita, K.S. Visualizing mechanical tension across membrane receptors with a fluorescent sensor. *Nature Methods* **9**, 64-U172 (2012).
13. Zhang, Y., Ge, C., Zhu, C. & Salaita, K. DNA-based digital tension probes reveal integrin forces during early cell adhesion. *Nat Commun* **5**, 5167 (2014).
14. Galior, K., Liu, Y., Yehl, K., Vivek, S. & Salaita, K. Titin-Based Nanoparticle Tension Sensors Map High-Magnitude Integrin Forces within Focal Adhesions. *Nano Lett* **16**, 341-348 (2016).
15. Liu, Y. *et al.* DNA-based nanoparticle tension sensors reveal that T-cell receptors transmit defined pN forces to their antigens for enhanced fidelity. *Proc Natl Acad Sci U S A* (2016).
16. Loidolt-Kruger, M. in Physics of Biological and Complex Systems, Vol. Doctor rerum naturalium (International Max Planck Research School, 2018).
17. Deng, S. *et al.* Effects of donor and acceptor's fluorescence lifetimes on the method of applying Forster resonance energy transfer in STED microscopy. *J Microsc* **269**, 59-65 (2018).
18. Holzmeister, P., Wunsch, B., Gietl, A. & Tinnefeld, P. Single-molecule photophysics of dark quenchers as non-fluorescent FRET acceptors. *Photochem Photobiol Sci* **13**, 853-858 (2014).
19. Le Reste, L., Hohlbein, J., Gryte, K. & Kapanidis, A.N. Characterization of dark quencher chromophores as nonfluorescent acceptors for single-molecule FRET. *Biophys J* **102**, 2658-2668 (2012).

20. Schnitzbauer, J., Strauss, M.T., Schlichthaerle, T., Schueder, F. & Jungmann, R. Super-resolution microscopy with DNA-PAINT. *Nat Protoc* **12**, 1198-1228 (2017).
21. Jungmann, R. *et al.* Single-molecule kinetics and super-resolution microscopy by fluorescence imaging of transient binding on DNA origami. *Nano Lett* **10**, 4756-4761 (2010).
22. Whitley, K.D., Comstock, M.J. & Chemla, Y.R. Elasticity of the transition state for oligonucleotide hybridization. *Nucleic Acids Res* **45**, 547-555 (2017).
23. Woodside, M.T. *et al.* Nanomechanical measurements of the sequence-dependent folding landscapes of single nucleic acid hairpins. *Proc Natl Acad Sci U S A* **103**, 6190-6195 (2006).
24. Whitley, K.D., Comstock, M.J. & Chemla, Y.R. Elasticity of the transition state for oligonucleotide hybridization. *Nucleic Acids Res.* **45**, 547-555 (2017).
25. Bell, G.I. Models for the specific adhesion of cells to cells. *Science* **200**, 618-627 (1978).
26. Petrosyan, R. Improved approximations for some polymer extension models. *Rheologica Acta* **56**, 21-26 (2017).
27. Morimatsu, M., Mekhdjian, A.H., Adhikari, A.S. & Dunn, A.R. Molecular tension sensors report forces generated by single integrin molecules in living cells. *Nano Lett* **13**, 3985-3989 (2013).
28. Rust, M.J., Bates, M. & Zhuang, X. Sub-diffraction-limit imaging by stochastic optical reconstruction microscopy (STORM). *Nat Methods* **3**, 793-795 (2006).
29. Betzig, E. *et al.* Imaging intracellular fluorescent proteins at nanometer resolution. *Science* **313**, 1642-1645 (2006).
30. Heilemann, M. *et al.* Subdiffraction-resolution fluorescence imaging with conventional fluorescent probes. *Angew Chem Int Ed Engl* **47**, 6172-6176 (2008).
31. Jungmann, R. *et al.* Multiplexed 3D cellular super-resolution imaging with DNA-PAINT and Exchange-PAINT. *Nat Methods* **11**, 313-318 (2014).
32. Kong, F., Garcia, A.J., Mould, A.P., Humphries, M.J. & Zhu, C. Demonstration of catch bonds between an integrin and its ligand. *J Cell Biol* **185**, 1275-1284 (2009).
33. Chen, Y. *et al.* An integrin alphaIIbbeta3 intermediate affinity state mediates biomechanical platelet aggregation. *Nat Mater* **18**, 760-769 (2019).
34. Schueder, F. *et al.* An order of magnitude faster DNA-PAINT imaging by optimized sequence design and buffer conditions. *Nat Methods* (2019).
35. Kloczewiak, M., Timmons, S. & Hawiger, J. Recognition site for the platelet receptor is present on the 15-residue carboxy-terminal fragment of the gamma chain of human fibrinogen and is not involved in the fibrin polymerization reaction. *Thromb. Res.* **29**, 249-255 (1983).
36. Farrell, D.H., Thiagarajan, P., Chung, D.W. & Davie, E.W. Role of fibrinogen alpha and gamma chain sites in platelet aggregation. *Proc. Natl. Acad. Sci. USA* **89**, 10729-10732 (1992).
37. Brockman, J.M. *et al.* Mapping the 3D orientation of piconewton integrin traction forces. *Nat Methods* **15**, 115-118 (2018).
38. Zhang, Y. *et al.* Platelet integrins exhibit anisotropic mechanosensing and harness piconewton forces to mediate platelet aggregation. *Proc Natl Acad Sci U S A* **115**, 325-330 (2018).
39. Xiao, T., Takagi, J., Coller, B.S., Wang, J.H. & Springer, T.A. Structural basis for allostery in integrins and binding to fibrinogen-mimetic therapeutics. *Nature* **432**, 59-67 (2004).
40. Zhang, K. & Chen, J. The regulation of integrin function by divalent cations. *Cell Adh Migr* **6**, 20-29 (2012).

41. Zhu, J. *et al.* Closed headpiece of integrin alphaIIbbeta3 and its complex with an alphaIIbbeta3-specific antagonist that does not induce opening. *Blood* **116**, 5050-5059 (2010).
42. Gawaz, M., Ott, I., Reininger, A.J. & Neumann, F.J. Effects of magnesium on platelet aggregation and adhesion. Magnesium modulates surface expression of glycoproteins on platelets in vitro and ex vivo. *Thromb. Haemost.* **72**, 912-918 (1994).
43. Ravn, H.B., Kristensen, S.D., Vissinger, H. & Husted, S.E. Magnesium inhibits human platelets. *Blood Coagul. Fibrinolysis* **7**, 241-244 (1996).
44. Gawaz, M., Reininger, A. & Neumann, F.J. Platelet function and platelet-leukocyte adhesion in symptomatic coronary heart disease. Effects of intravenous magnesium. *Thromb. Res.* **83**, 341-349 (1996).
45. Gries, A. *et al.* The effect of intravenously administered magnesium on platelet function in patients after cardiac surgery. *Anesth Analg* **88**, 1213-1219 (1999).
46. Plow, E.F., Haas, T.A., Zhang, L., Loftus, J. & Smith, J.W. Ligand binding to integrins. *J. Biol. Chem.* **275**, 21785-21788 (2000).
47. Hu, D.D., Barbas, C.F. & Smith, J.W. An allosteric Ca2+ binding site on the beta3-integrins that regulates the dissociation rate for RGD ligands. *J. Biol. Chem.* **271**, 21745-21751. (1996).
48. Takagi, J., Petre, B.M., Walz, T. & Springer, T.A. Global conformational rearrangements in integrin extracellular domains in outside-in and inside-out signaling. *Cell* **110**, 599-611 (2002).
49. Stuiver, I., Ruggeri, Z. & Smith, J.W. Divalent cations regulate the organization of integrins alpha v beta 3 and alpha v beta 5 on the cell surface. *J Cell Physiol* **168**, 521-531 (1996).